Dynamical encircling of the exceptional point in a largely detuned multimode optomechanical system

Dan Long,[1,*] Xuan Mao,[1,*] Guo-Qing Qin,[1] Hao Zhang,[2] Min Wang ⊚,[3] Gui-Qin Li,[1,4] and Gui-Lu Long ⊚[1,3,4,5,6,†]

[1]*Department of Physics, State Key Laboratory of Low-Dimensional Quantum Physics, Tsinghua University, Beijing 100084, China*
[2]*Purple Mountain Laboratories, Nanjing 211111, China*
[3]*Beijing Academy of Quantum Information Sciences, Beijing 100193, China*
[4]*Frontier Science Center for Quantum Information, Beijing 100084, China*
[5]*Beijing National Research Center for Information Science and Technology, Beijing 100084, China*
[6]*School of Information, Tsinghua University, Beijing 100084, China*

Dynamical encircling of the exceptional point (EP) reveals a number of intriguing physical phenomena and their potential applications. To enrich the manipulations of optical systems in experiments, we study the dynamic encircling of the EP, that is, the state transfer process, in a largely detuned multimode optomechanical system. The process of state transfer has been investigated with different factors regarding the location of the start point, orientation, and initial state of the trajectories around the EP in the parameter space. The results show that nonreciprocal and chiral topological energy transfers between two optical modes are performed successfully by tuning the effective optomechanical coupling into a multimode system with large detuning. Moreover, the evolution speed of the system parameters is also discussed. Our work demonstrates the fundamental physics of the EP in the large detuning domain of a multimode optomechanical system and provides an alternative for manipulating optical modes in non-Hermitian systems.

I. INTRODUCTION

Exceptional points (EPs) [1,2], that is, non-Hermitian degeneracy points at which eigenvalues and eigenvectors coalesce simultaneously [3], have been promoted in recent years [4,5]. Significantly different from diabolic points (DPs), whose eigenvalues coalesce while the associated eigenvectors can be designated as orthogonal in a Hermitian system [6], plenty of practical applications [5,7–15] have used EPs, such as phonon lasers [8–10] and ultrasensitive sensors [5,7,11–14]. Systems evolving near EPs, for example, EP-based devices [16–18], exhibit numerous physical phenomena, including nonreciprocal topological energy transfer [4,19], whereas systems evolving near DPs only result in a geometric phase [6]. In particular, dynamically encircling an EP [20] provides opportunities to realize asymmetric mode switching [4,21], which has been exhibited in various systems such as waveguides [22], circuits [23], and plasmonics [24,25]. Owing to their ability to enhance light and matter interactions in ultrasmall volumes, high-quality microcavities [26,27] have been a promising platform for manipulating EPs to approach state conversion [2,28], which has been experimentally demonstrated [19]. Determined by the orientation, location, and initial state, dynamically encircling an EP presents outstanding robustness [4] and chirality [29].

For the experimental realization of an EP in the microcavity optical mode, the two optical cavities are typically direct coupled [1]. According to previous research, only laser detuning and optical-optical coupling strength can be employed to tune the entire system [30,31], whereas it is difficult to control the coupling strength between optical modes. The lack of control measurements limits the ability to dynamically encircle the EP, and additional degrees of parameter control are required. To solve this problem, optomechanical systems [32–42], where an auxiliary mechanical mode can be introduced to achieve indirect coupling between the two optical modes, have recently been proposed and experimentally realized [43–45]. Through indirect coupling, the methods of regulating EPs become more abundant.

In this study, to enrich the manipulation potential of optical systems in dynamically encircling EPs, we propose a largely detuned multimode optomechanical system to achieve a strong-coupling regime with the aid of an optomechanical dark mode. The effect of the initial state, orientation, location, and velocity on the time-dependent system dynamic evolution is investigated and its track is a closed loop in the parameter space. The results show that state conversion may occur whether or not the path encloses the EP because of the effect of non-Hermiticity-induced nonadiabatic transition (NAT) [46,47], whereas chirality conversion will occur if the path encloses the EP. Moreover, the nonreciprocity and chirality of the topological energy-transform efficiency depend on the locations of the control loops in the parameter space. Our work may inspire further experiments on photon state manipulation in the detuning domains of multimode optomechanical systems and devices based on extended non-Hermitian photonic architecture.

The remainder of this article is organized as follows: In Sec. II, we demonstrate the basic model and Hamiltonian of the system. We discuss the dynamic evolution of the system in Sec. III and the topological energy transfer in Sec. IV. The

---

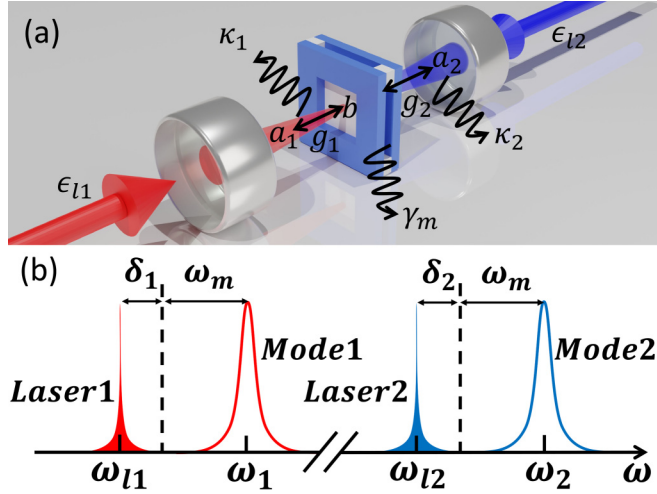*These authors contributed equally to this work.
†gllong@tsinghua.edu.cn

FIG. 1. (a) Schematic of the optomechanical system composed of two optical modes (a_1 and a_2) and one mechanical mode (b). The two optical modes are coupled with the mechanical modes simultaneously. (b) Frequency spectrum of the two optical systems and two strong power lasers with red detunings.
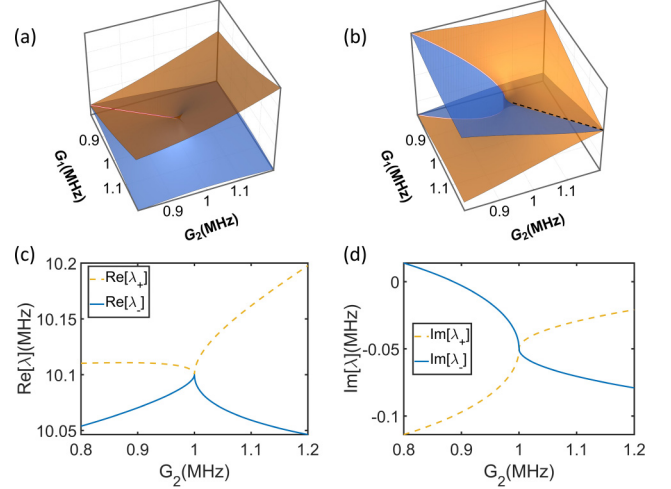

FIG. 2. (a) Real part $\mathrm{Re}[\lambda_\pm]$ and (b) imaginary part $\mathrm{Im}[\lambda_\pm]$ of the effective Hamiltonian eigenvalues as functions of the optomechanical coupling strengths G_1 and G_2. The black dashed line describes where the imaginary parts of the eigenvalues coalesce. (c) Real part $\mathrm{Re}[\lambda_\pm]$ and (d) imaginary part $\mathrm{Im}[\lambda_\pm]$ of the effective Hamiltonian eigenvalues as functions of the optomechanical coupling strength G_2 with G_1 fixing at G. Yellow dashed (blue solid) line corresponds to the eigenvalue $\lambda_+(\lambda_-)$. $\delta_1 = \delta_2 = 10G = 10$ MHz, $\kappa_1 = 0.3G = 0.3$ MHz, and $\kappa_2 = -0.1G = -0.1$ MHz are the parameters of the effective Hamiltonian.

conclusions are presented in Sec. V. The Appendix presents how to choose independent variables of the control loop.

II. MODEL AND HAMILTONIAN

A schematic representation of the proposed system is shown in Fig. 1(a), composed of two optical modes and one mechanical mode. The mechanical mode can be a film that is fixed to the left and right. The two optical modes were driven by strong lasers with central frequencies of ω_{l1} and ω_{l2}. The damping (gaining) rates of the optical modes were κ_j, and the mechanical mode was γ. The mechanical mode was simultaneously and dispersively coupled with the two optical modes. The system Hamiltonian can be described by

$$H = H_{\mathrm{free}} + H_{\mathrm{int}} + H_{\mathrm{drive}}, \quad (1)$$

where

$$H_{\mathrm{free}} = \omega_1 a_1^\dagger a_1 + \omega_2 a_2^\dagger a_2 + \omega_m b^\dagger b,$$

$$H_{\mathrm{int}} = g_1 a_1^\dagger a_1 (b^\dagger + b) + g_2 a_2^\dagger a_2 (b^\dagger + b),$$

$$H_{\mathrm{drive}} = i\sqrt{\kappa_{ex1}}\epsilon_{l1} e^{-i\omega_{l1}t} a_1^\dagger + i\sqrt{\kappa_{ex2}}\epsilon_{l2} e^{-i\omega_{l2}t} a_2^\dagger + \mathrm{H.c.}, \quad (2)$$

in which ω_j denotes the resonance frequency of the jth optical mode and ω_m describes the resonance frequency of the mechanical mode. a_j and b are the annihilations of the jth optical mode and mechanical mode, respectively; g_j and κ_{exj} describe the single-photon optomechanical coupling rate and coupling damping rate, respectively; and ϵ_{lj} is the power of the jth laser.

In the interaction picture of the driving field, the Hamiltonian is changed to

$$H = \omega_m b^\dagger b - \sum_{j=1,2} [\Delta_j a_j^\dagger a_j - g_j a_j^\dagger a_j (b^\dagger + b)]$$
$$+ i\sqrt{\kappa_{ex1}}\epsilon_{l1} a_1^\dagger + i\sqrt{\kappa_{ex2}}\epsilon_{l2} a_2^\dagger, \quad (3)$$

where $\Delta_j = \omega_{lj} - \omega_j$ denotes the detuning between the optical modes and corresponding driving fields. It is convenient to solve the nonlinear Heisenberg equations if the Hamiltonian above is linearized. The annihilation of the optical modes can be changed by $a_j \to \overline{a_j} + \delta a_j$. The linearized Hamiltonian is converted to

$$H = \omega_m b^\dagger b - \sum_{j=1,2} [\Delta_j a_j^\dagger a_j - G_j(a_j^\dagger + a_j)(b^\dagger + b)], \quad (4)$$

where $G_j = g_j \overline{a_j}$ describes the optically driven coupling between the mechanical mode and cavity mode j, and $\overline{a_j} = \sqrt{\kappa_{exj}}\epsilon_{lj}/(-i\Delta_j + \frac{\kappa_j}{2})$ is the average annihilation. In the following, we focus on the strong-coupling regime, that is, $G_j > (\kappa_j, \gamma_m)$ and the typical limit $\kappa_j \gg \gamma_m$.

The case in which both optical modes are driven under red sidebands is considered. For convenience, the detuning can be converted to $\delta_j = -\Delta_j - \omega_m$. Under the condition $\omega_m \gg (\delta_j, G_j)$ and the rotating-wave approximation, the Hamiltonian can be written as $H_A = \sum_{j=1,2} [\delta_j a_j^\dagger a_j + G_j(a_j^\dagger b + a_j b^\dagger)]$ in the interaction picture of $\omega_m(b^\dagger b + \sum_{j=1,2} a_j^\dagger a_j)$. For large detuning conditions $\delta_j \gg G_j$, mechanical modes can be eliminated [44] and we obtain the effective Hamiltonian as

$$\mathcal{H} = \begin{pmatrix} \delta_1 + \Omega_1 - \frac{\kappa_1}{2}i & \Omega \\ \Omega & \delta_2 + \Omega_2 - \frac{\kappa_2}{2}i \end{pmatrix}, \quad (5)$$

where $\Omega_j = G_j^2/\delta_j$ is the resonance ac-Stark shift of cavity mode j, and $\Omega = G_1 G_2(\delta_1^{-1} + \delta_2^{-1})/2$ describes the effective coupling between the two optical modes [44].
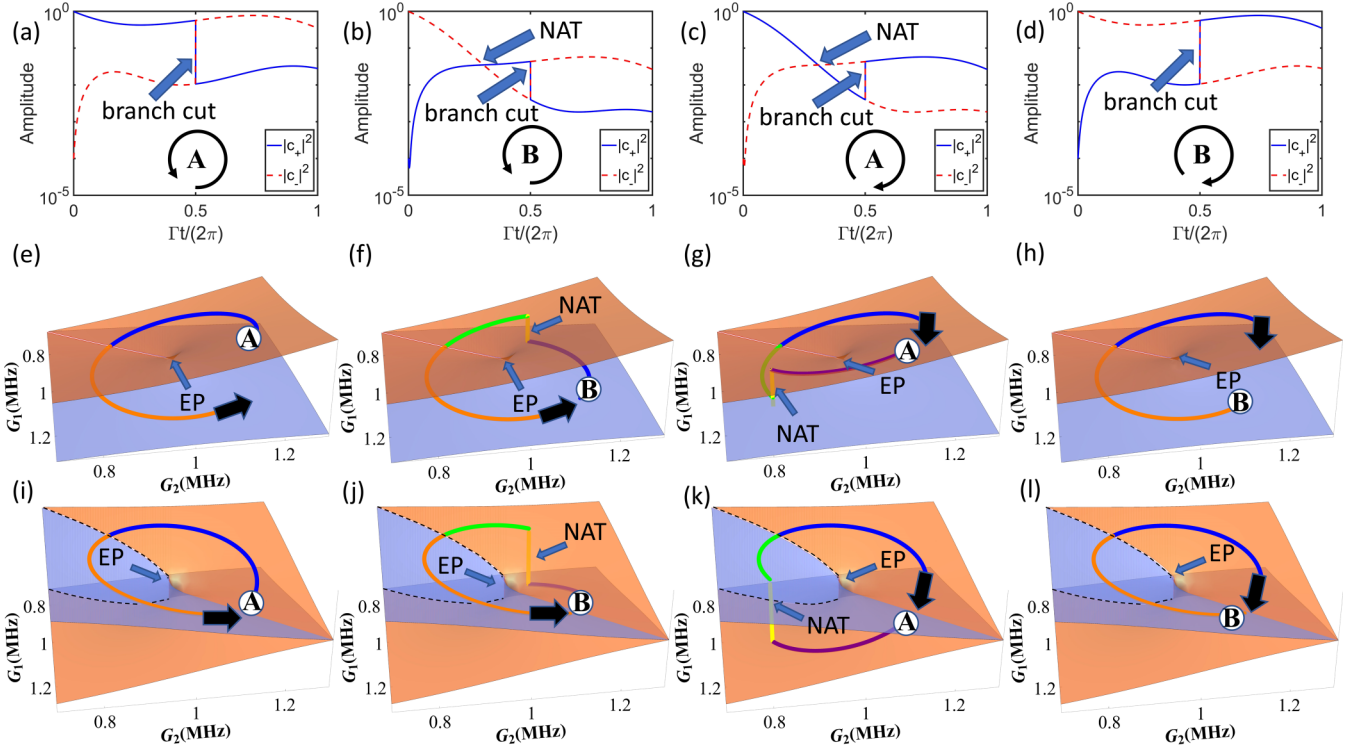
FIG. 3. (a)–(d) Instantaneous amplitudes of eigenstates during the loop evolution that encloses the EP. The blue solid line describes the amplitude of λ_+, and the red dashed line describes the amplitude of λ_-. (a) and (b) are the case where the loop orientation is CCW, whereas (c) and (d) are the case where the loop orientation is CW. Point A (B) corresponds to the case that the initial state is nearly $|\lambda_+\rangle$ ($|\lambda_-\rangle$). (a) and (c) are the case where the initial state is A, whereas (b) and (d) are the case where the initial state is B. (e)–(h) The encircling path on the real part of the eigenstates of the Hamiltonian corresponding to (a)–(d). (i)–(l) The encircling path on the imaginary part of the eigenstates of the Hamiltonian corresponding to (a)–(d). The blue (orange) Riemann sheet is the imaginary part of λ_- (λ_+). The black dashed lines denote the branch cut of the two imaginary parts of the eigenvalue Riemann sheets. The color of the path corresponds to the different stages of the evolution. The parameters of the effective Hamiltonian are the same as those in Fig. 2(b).

The eigenvalues of the effective Hamiltonian in Eq. (5) can be obtained as

$$\lambda_\pm = \frac{1}{2}(A_1 + A_2) \pm \frac{\sqrt{(A_1 - A_2)^2 + 4\Omega^2}}{2}, \quad (6)$$

where $A_j = \delta_j + \Omega_j - \frac{\kappa_j}{2}i$. It is clear that the effective Hamiltonian in Eq. (5) has an EP if the conditions $\delta_1 + \Omega_1 = \delta_2 + \Omega_2$ and $\Omega = |\kappa_1 - \kappa_2|/4$ are satisfied. If the conditions under which the loss and gain of the two optical modes are balanced, that is, $\kappa_1 = -\kappa_2$, and $\delta_1 + \Omega_1 = \delta_2 + \Omega_2$ is satisfied, the effective Hamiltonian in Eq. (5) will exhibit $\mathcal{PT}$ symmetry.

The real and imaginary parts of the eigenvalues are shown in Figs. 2(a) and 2(b). G_1 and G_2 were chosen as independent variables, which could be tuned by changing the powers of the two driving lasers. The choice of these two independent variables is described in length in the Appendix. In short, this set of dependent parameters is the best choice for showing the structure of the effective Hamiltonian. It is easy to calculate that an EP exists when $G_1 = G_2 = G = 1$ MHz since the eigenvalues λ_+ and λ_- coalesce at the EP. Near the EP, the real and imaginary parts of the eigenvalues exhibit the same structure as the Riemann sheets of the complex square-root function $z^{\frac{1}{2}}$. On the basis of Figs. 2(a) and 2(b), G_1 is fixed at G and the only independent variable is G_2. The real and imaginary parts of the effective Hamiltonian eigenvalues as functions of G_2 are shown in Figs. 2(c) and 2(d), respectively.

In these two subgraphs, it can be seen that when $G_2 \neq G$, the real and imaginary parts of the eigenvalues are distinct, whereas when $G_2 = G$, the real and imaginary parts of the eigenvalues are identical.

III. DYNAMICALLY ENCIRCLING AN EXCEPTIONAL POINT

The dynamic evolution of the operators depends on the Heisenberg equation $\frac{dA}{dt} = \frac{i}{\hbar}[H, A]$. Owing to the special structure of the Riemann sheets shown in Figs. 2(a) and 2(b), when G_1 and G_2 vary around a closed loop, the evolution results differ depending on whether the loop encloses the EP. Curiously, the evolution results depend not only on whether the loop encloses the EP, but also on the orientation of the loop, initial state of the loop, and velocity of the evolution.

To realize the dynamic evolution of the Hamiltonian in parametric space, G_1 and G_2 were tuned by changing the powers of the two input lasers ϵ_{l1} and ϵ_{l2}. If we denote $|\lambda_+(t)\rangle$ and $|\lambda_-(t)\rangle$ as the instantaneous eigenvectors of the time-dependent Hamiltonian, the time-dependent state can be expressed as $|\psi(t)\rangle = c_+(t)|\lambda_+(t)\rangle + c_-(t)|\lambda_-(t)\rangle$, where c_+ and c_- denote the amplitudes of the instantaneous eigenvalues and continuously follow the instantaneous basis during the new basis. Owing to the non-Hermitian Hamiltonian, the instantaneous eigenvectors are not orthogonal,
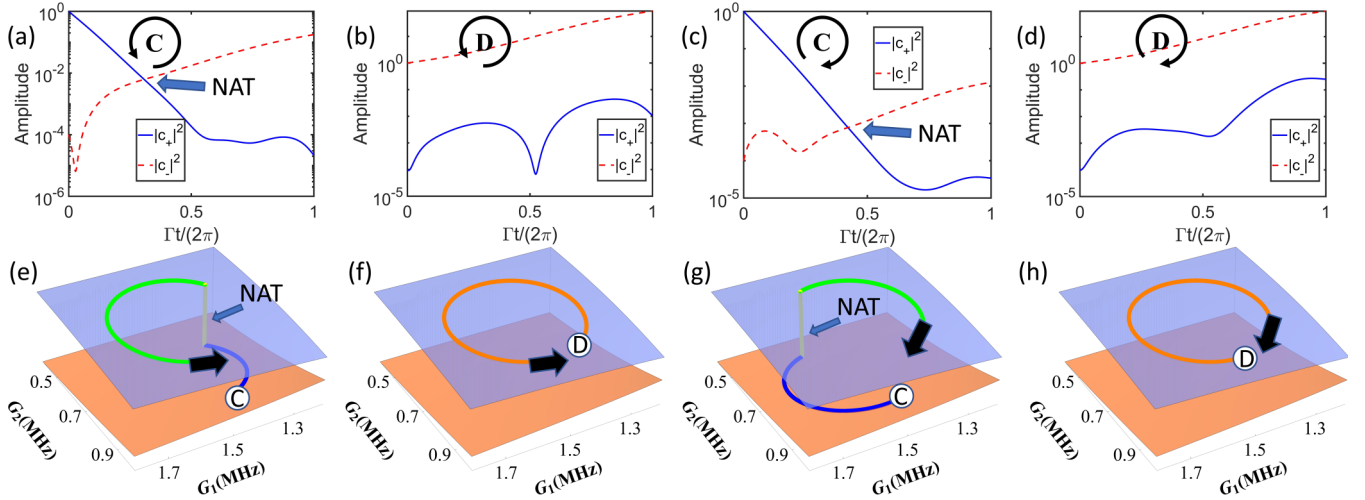
FIG. 4. (a)–(d) Instantaneous amplitudes of eigenstates during the loop evolution that do not enclose the EP. The blue solid line describes the amplitude of λ_+, whereas the red dashed line describes the amplitude of λ_-. (a) and (b) are the case where the loop orientation is CCW, whereas (c) and (d) are the case where the loop orientation is CW. Point C (D) corresponds the case that the initial state is nearly $|\lambda_+\rangle$ ($|\lambda_-\rangle$). (a) and (c) are the case where the initial state is C, whereas (b) and (d) are the case where the initial state is D. (e)–(h) The encircling path on the imaginary part of the eigenstates of the Hamiltonian corresponding to (a)–(d). The blue (orange) Riemann sheet is the imaginary part of λ_- (λ_+). The color of the path corresponds to the different stages of the evolution. The parameters of the effective Hamiltonian are the same as those in Fig. 2(b).

that is, $\langle \lambda_- | \lambda_+ \rangle \neq 0$. Therefore, the instantaneous eigenvalue amplitudes cannot be obtained directly. This can be expressed as $c_+(t) \neq \langle \lambda_+(t) | \psi(t) \rangle$ and $c_-(t) \neq \langle \lambda_-(t) | \psi(t) \rangle$. To obtain the amplitudes, new vectors $|l_\pm(t)\rangle = |\lambda \pm (t)\rangle - \langle \lambda \mp (t) | \lambda \pm (t) \rangle | \lambda \mp (t) \rangle$ can be established; then the amplitudes can be determined by projecting the state after evolution onto the new vectors $c_+(t) = \frac{\langle l_+(t) | \psi(t) \rangle}{1 - |\langle \lambda_-(t) | \lambda_+(t) \rangle|^2}$, $c_-(t) = \frac{\langle l_-(t) | \psi(t) \rangle}{1 - |\langle \lambda_-(t) | \lambda_+(t) \rangle|^2}$ [48].

It is convenient to obtain the evolution information by observing the instantaneous amplitudes of the eigenvalues. The simplest function of the loop is expressed as $G_1(t) = \alpha_1 G_1^{EP} + \beta_1 G_1^{EP} \cos(\Gamma t + \phi_0)$ and $G_2(t) = \alpha_2 G_2^{EP} + \beta_2 G_2^{EP} \sin(\Gamma t + \phi_0)$. The system obtains an EP when G_i approaches G_i^{EP}. Γ describes the velocity of evolution and its sign describes the orientation of the loop. $\Gamma > 0$ corresponds to a counterclockwise (CCW) loop, whereas $\Gamma < 0$ corresponds to a clockwise (CW) loop. α_i determines the location of the loop center and β_i determines the radius of the loop. The phase of the starting point is determined by ϕ_0 when we determine that the time interval is $[0, \frac{2\pi}{|\Gamma|}]$. In the cases where the loop encloses the EP, the starting point is selected where the imaginary parts of the eigenvalues coalesce. Without loss of generality, it is assumed that most of the energy is initially concentrated on one of the eigenstates, that is, $c_+(0) \gg c_-(0)$ or $c_-(0) \gg c_+(0)$. These conditions correspond to the initial time $t = 0$ in the subgraphs in Figs. 3(a)–3(d) and Figs. 4(a)–4(d).

It is necessary to study the case in which the loop encloses the EP and the evolution is adiabatic. $\alpha_1 = \alpha_2 = 1$ and $\beta_1 = \beta_2 = 0.2$ can make the loop enclose the EP. $\Gamma = 0.1G$ ensures that the evolution is adiabatic, and $\phi_0 = \frac{\pi}{4}$ causes the starting point to be where the imaginary parts of the eigenvalues coalesce. From Figs. 3(a) to 3(d), there is a state flip when $\Gamma t/(\pi) = 1$. This is a direct result of the topological

structure of the imaginary parts of the eigenvalues around the EP. When the time approaches $\Gamma t/(\pi) \to 1$, if the state wants to remain unchanged, the imaginary part of the state will change abruptly because of the branch cut, which connects two Riemann sheets of imaginary parts of the eigenvalues. Therefore, the path will go to another Riemann sheet from the previous Riemann sheet via branch cut, which is shown by the black dashed line in Figs. 3(i)–3(l). In Figs. 3(b) and 3(c), NAT occurs and the state evolves to another sheet adiabatically. Because of the time-dependent Hamiltonian, the state will not precisely be the eigenstate of the instantaneous Hamiltonian during the evolution. If the state first propagates on the higher-loss sheet, the evolution will be unstable, and if the evolution is adiabatic, the state will gradually propagate to the lower-loss sheet. When $c_+(t_1) = c_-(t_1)$, we define it as the confirmation of the occurrence of NAT at time $t = t_1$ [47]. The yellow part of the path, shown in Figs. 3(j) and 3(k), exhibits the NAT during the evolution. In Fig. 3(b), the state first propagates on the blue sheet, which is higher loss now, and after a time delay, the state will propagate to the orange sheet, which is lower loss now. In Fig. 3(c), although the initial state is different from the case in Fig. 3(b), the orientation of the loop is opposite that of Fig. 3(b) and there is also a NAT.

It is easy to see that if the loop orientation is CCW, the final state will evolve to $|\lambda_-\rangle$ regardless of the initial state. If the loop orientation is CW, the final state evolves to $|\lambda_+\rangle$ regardless of the initial state being $|\lambda_+\rangle$ or $|\lambda_+\rangle$. We can also find that whether the final state is different from the initial state corresponds to whether NAT has occurred.

To summarize, after the loop evolves to enclose the EP, the results are determined by the orientation of the loop and the initial state. Because different evolution orientations correspond to different evolution results, chirality occurs in the state conversion.
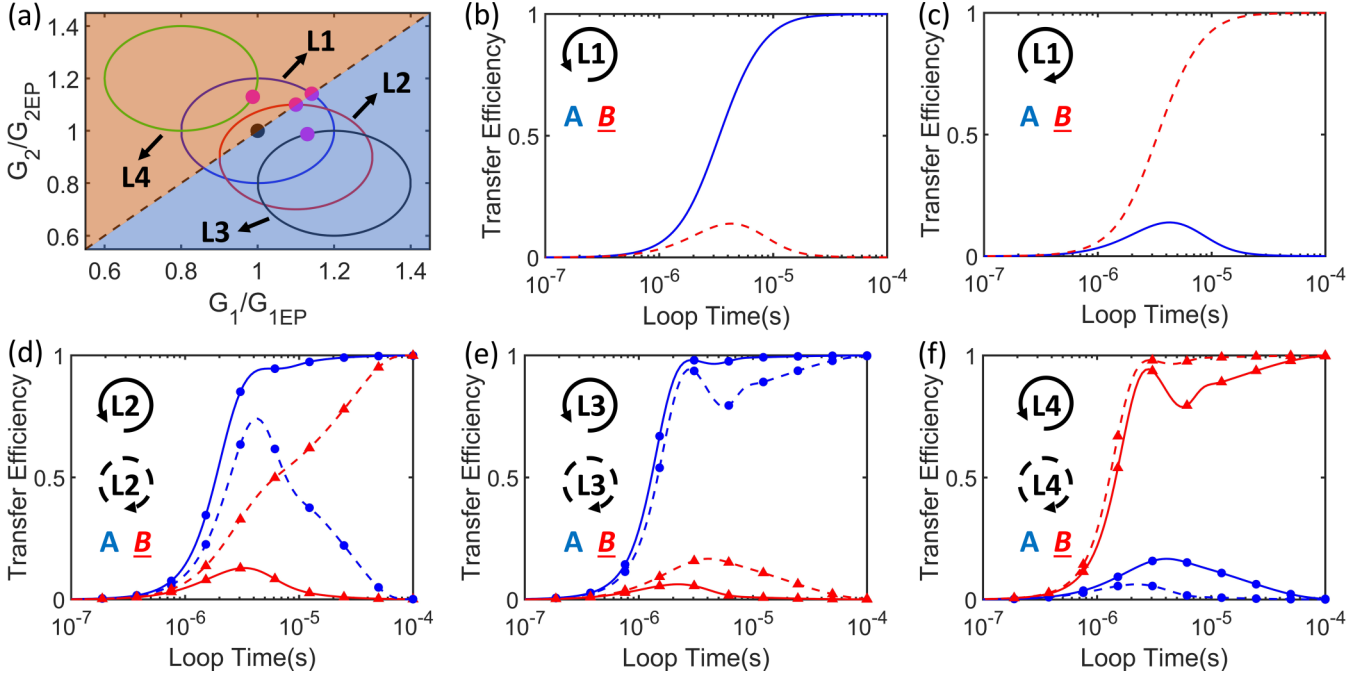
FIG. 5. (a) Parametric space of the system. There are four different loops marked L1–L4 in this subgraph. The black dashed line $G_1 = G_2$ is the demarcation line for the less lossy region of the eigenvalues. The orange (blue) area represents the area where the damping rate of the eigenvalue $\lambda_+(\lambda_-)$ is smaller. The black dot denotes the location of the EP and the magenta dots denote the starting points location. (b),(c) The energy transfer efficiency E as a function of the period τ on the loop L1 described in (a). The blue solid (red dashed) solid line is the transfer efficiency E_+ (E_-) where the state $|\lambda_+\rangle$ ($|\lambda_-\rangle$) is initially driven, corresponding to the initial state at A ($\underline{B}$). The loop orientation in (b) and (c) is CCW and CW, respectively. (d)–(f) The energy transfer efficiency E as a function of the period τ on the loops L2–L4 described in (a). The blue circle (red triangle) solid line is the transfer efficiency E_+ (E_-) where the initial state is at A ($\underline{B}$) and the orientation is CCW, whereas the blue circle (red triangle) dashed line is the transfer efficiency E_+ (E_-), which is the initial state at A ($\underline{B}$) and orientation of CW. The parameters of the effective Hamiltonian are the same as those in Fig. 2(b).

The case in which the loop does not enclose the EP is required for comparison with the case above. The evolution is also adiabatic. If $\alpha_1 = 1.5$, $\alpha_2 = 0.5$, and $\beta_1 = \beta_2 = 0.2$, the loop will not enclose the EP. $\Gamma = 0.1G$ ensures that the evolution is adiabatic. Figures 4(a) and 4(c) show that there is a state flip during the loop evolution, whereas there is no state flip in Figs. 4(b) and 4(d). In Figs. 4(a) and 4(c), the initial state first evolves on a higher-loss sheet and NAT will happen after a time delay so the final state will be different from the initial state. In Figs. 4(b) and 4(d), the state keeps in the lower-loss sheet and NAT does not occur. Regardless of the initial state, the final state must be the state on the lower-loss Riemann sheet, which is $|\lambda_-\rangle$ in this case.

To summarize, if the loop does not enclose the EP, there will be no state flip because of the topological structure of the Riemann sheet around the EP, and there is no chirality in the state conversion. However, owing to the NAT effect, state conversion may occur if the initial state is initially on the higher-loss Riemann sheet.

IV. TOPOLOGICAL ENERGY TRANSFER

From Figs. 3 and 4, it is evident that the energy of the system was lost or gained during the loop evolution. This phenomenon shows that the total damping rate of the system may be positive or negative, depending on the sign of the imaginary parts of the instantaneous eigenvalues. We studied the dynamic evolution under different conditions regarding loop orientation, initial state, and whether the loop encloses the EP. Here, we investigated the inflection of the loop velocity on evolution. The evolutions in Figs. 3 and 4 are adiabatic, such that the period of the loop τ should satisfy $\tau \gg 1/|\lambda_+ - \lambda_-|$ [19]. Whether the loop is adiabatic determines the energy-transfer results.

To focus on the energy transfer during the loop, we examined the relative energy before and after the evolution. When most of the energy is contributed in the state $|\lambda_+(0)\rangle$, the energy-transfer efficiency is defined as $E_+ = \frac{|c_-(\tau)|^2}{|c_+(\tau)|^2 + |c_-(\tau)|^2}$. In contrast, when most of the energy is contributed in the state $|\lambda_-(0)\rangle$, the energy transfer efficiency is defined as $E_- = \frac{|c_+(\tau)|^2}{|c_+(\tau)|^2 + |c_-(\tau)|^2}$.

In Fig. 5(a), L1–L4 are four different loops to be investigated, whose parameters are declared in Table I. ϕ_0 in L1 and L2 ensured that the starting points were at the place where the imaginary parts of the eigenvalues coalesce. In Figs. 5(b)–5(f), when the period of the loop was sufficiently small ($\tau \to 0$), no matter which state is initially driven and what the orientation is, the transfer efficiency was negligible ($E \to 0$). This explains why a sudden perturbation of the system was insufficient to cause a switch in states.

Figures 5(b)–5(d) represent the scenario where the loop encloses the EP. As the period of the loop increased, it can be

TABLE I. The parameters of the loops of L1–L4 as shown in Fig. 5(a).

Parameters of loops	L1	L2	L3	L4
α_1	1	1.1	1.2	0.8
α_2	1	0.9	0.8	1.2
β_1	0.2	0.2	0.2	0.2
β_2	0.2	0.2	0.2	0.2
Include EP?	Yes	Yes	No	No

seen that the transfer efficiencies E_+ and E_- both increased. When the loop orientation was CCW, the transfer efficiency E_+ increased to 1 as the loop evolution was adiabatic ($\tau \gg 1$ μs), whereas the transfer efficiency E_- would go to zero after a maximum was reached. When the loop orientation was CW, the transfer efficiency E_- increased to 1 as the loop evolution was adiabatic ($\tau \gg 1$ μs), whereas the transfer efficiency E_+ would go to zero after reaching a maximum. Rapid evolution causes vanishing transfer efficiency, whereas adiabatic evolution results in a different transfer efficiency, which depends on the loop orientation. These phenomena reflect the nonreciprocity of each topological operation.

Figures 5(e) and 5(f) represent the scenario where the loop does not enclose the EP. As the period of the loop increased, it can be seen that the transfer efficiencies E_+ and E_- both increased. When the loop was L3, the transfer efficiency E_+ increased to 1 as the loop evolution was adiabatic ($\tau \gg 1$ μs), whereas the transfer efficiency E_- would go to zero after a maximum is reached. When the loop was L4, the transfer efficiency E_- increased to 1 as the loop evolution was adiabatic ($\tau \gg 1$ μs), whereas the transfer efficiency E_+ would go to zero after reaching a maximum. It is clear that whether the transfer efficiency increases to 1 depends on the location of the loop center, regardless of the loop orientation. This behavior was different when loops did or did not enclose the EP.

In Figs. 5(b) and 5(c), the loop L1 is symmetrical around the black dashed line, which is the demarcation line for the less-lossy region of the eigenvalues. It can be seen that the transfer efficiency behavior shows symmetry. The blue solid (red dashed) line in Fig. 5(b) is the same as the red dashed (blue solid) line in Fig. 5(c). In Fig. 5(d), the loop does not appear symmetrical around the black dashed line. The transfer efficiencies in the CW and CCW did not exhibit symmetry. It is evident that the transfer efficiency E_+ in L2 increased faster than that in loop L1 when the orientation was CCW. When the orientation was CW, the maximum value of E_+ in L2 was larger than that in the loop, which was symmetrical. These behaviors can be explained by the fact that the time when loop L2 goes through the region where the gain of $|\lambda_-\rangle$ is larger was longer than the time in the region where $|\lambda_+\rangle$ is less lossy. This causes asymmetry in the transfer efficiency. In Figs. 5(e) and 5(f), the adiabatic evolution behavior was mainly determined by the position of the center of the trajectory and had little to do with the orientation of the trajectory. This can be explained by the fact that because the loop does not contain the EP, the topological structure does not cause state conversion; only the NAT causes state conversion. The result of the evolution is not determined by

the orientation, but by the location and velocity of the loop. L3 (L4) was completely in the region where λ_- (λ_+) was less lossy, such that E_+ (E_-) approached 1 when the evolution was adiabatic.

To summarize, if the loop encloses the EP, the behavior of the energy-transfer efficiency depends not only on the orientation of the loop, but also on the location of the loop center. On the other hand, if the loop does not enclose the EP, the behavior is mainly determined by the location of the loop.

V. CONCLUSION

We demonstrated an optomechanical system composed of two optical modes and one mechanical mode. This system has an EP if certain conditions are satisfied. We then researched the dynamic evolution of a time-dependent system, whose track was a closed loop in the parametric space. Whether chirality existed in the state conversion was determined by whether the loop enclosed the EP, which reflected the topological structure around the EP and influenced the result of the dynamic evolution. We also found that the initial state and orientation affected the evolution result. In addition, we studied the impact of the evolution velocity and found that if the evolution was not adiabatic, the transfer efficiency was zero, regardless of the loop orientation. When the evolution was adiabatic, the transfer efficiency depended on the loop orientation. Furthermore, we found that the absolute location of the loop affected the transfer efficiency. Our findings enrich the understanding of the closed-path evolution of non-Hermitian systems, which will be beneficial to system control and broaden the scope of designing EP-based photonics devices. Combined with the results of this study, there is great significance in the future investigation of dynamic encircling around high-order EPs. In addition, it is hoped that the energy-transfer efficiency can be improved at a higher velocity in the control loop by applying machine learning to learn the results of the control loop around the EPs under different trajectory parameters.

APPENDIX: SELECTION OF INDEPENDENT VARIABLES

In Sec. II, we demonstrated the basic model and Hamiltonian of the system, and the dynamic evolution of the system was studied in Sec. III. Under the large detuning condition $\delta_j \gg G_j$, the mechanical modes can be eliminated such that variables G_j, δ_j, and κ_j can be used as independent variables. When the couplings between the fiber and optical modes are fixed, κ_j is not conveniently regulated as an inherent property of the system material. If two independent variables are
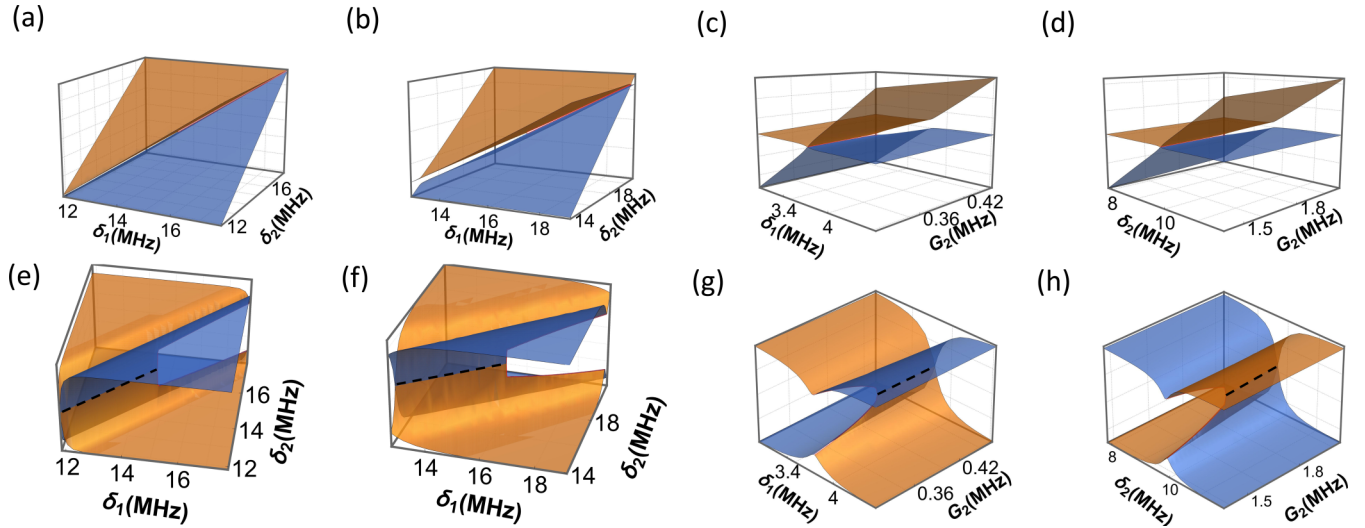
FIG. 6. (a)–(d) Real parts of the effective Hamiltonian with different independent variable sets. (e),(f) Imaginary parts of the effective Hamiltonian with different independent variable sets corresponding to (a)–(d). The values of the determined parameters were declared in Table II. The black dashed line describes where the imaginary parts of the eigenvalues coalesce.

required, then there are four variable combinations (δ_1, G_1), (δ_1, G_2), (δ_1, δ_2), and (G_1, G_2). In Figs. 2–4, G_1 and G_2 are chosen to be the independent variables considering the satisfaction of the detuning condition and the steepness of the imaginary parts of the eigenvalues.

Figure 6 shows the real and imaginary parts of the effective Hamiltonian with three different independent variable sets, where the values of determined parameters are declared in Table II. In Figs. 6(e) and 6(f), δ_1 and δ_2 are chosen. It can be observed that the imaginary part around the black dashed line in Fig. 6(e) is steeper than that in Fig. 6(f). However, for the other nonindependent variables shown in Fig. 6(f), the large detuning conditions that lead to the disappearance of the mechanical mode are more difficult to realize than those in Fig. 6(e). By contrast, the imaginary part around the black dashed line in Figs. 6(e) and 6(f) is steeper than that in Figs. 6(g) and 6(h). In the last four subplots, the independent variable set shown in Fig. 6(g) was chosen as the optimal solution. If Fig. 2(b), whose independent variable set is (G_1, G_2), is also taken into account, we find that the

imaginary part around the black dashed line in Fig. 2(b) is the flattest and the conditions are easier to realize. However, where the black dashed line corresponds to the imaginary part of the parameter space, the real parts of the eigenvalues are inconsistent. In Figs. 6(a)–6(d), it is shown that the flatter it is around the black dashed line in Figs. 6(e)–6(h), the larger the difference of the real parts of eigenvalues in that part of the parameter space.

To study the influence of the steepness of the imaginary part of the effective Hamiltonian on the evolution, we defined the differential of the imaginary part of the eigenvalues, $D_i = \frac{\mathrm{Im}[\lambda](i+1) - \mathrm{Im}[\lambda](i)}{dt}$. dt denotes the time interval between $\mathrm{Im}[\lambda](i+1)$ and $\mathrm{Im}[\lambda](i)$, which is a constant. Figure 7 shows the instantaneous amplitudes of eigenstates and differential of $\mathrm{Im}[\lambda]$ during the loop evolution with variable sets (δ_1, δ_2) and (G_1, G_2). It can be seen that if D_i is sufficiently large, it can cause a state conversion. In Fig. 7(a), we can find a state conversion when $\Gamma t/(\pi) \to 1$, which corresponds to the

TABLE II. The values of the determined parameters in Figs. 2(a) and 2(b) and in Figs. 6(a)–6(g). In the table below, $G = 1$ MHz.

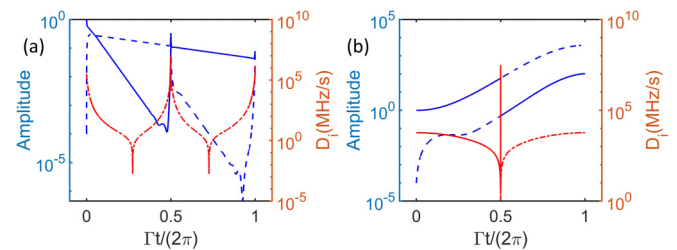| The tunable variable set	The values of determined parameters	The associated figures
(G_1, G_2)	$\delta_1 = \delta_2 = 10G$,	Fig. 2(a)
	$\kappa_1 = 0.3G, \kappa_2 = -0.1G$	Fig. 2(b)
(δ_1, δ_2)	$G_1 = G_2 = G$,	Fig. 6(a)
	$\kappa_1 = 0.3G, \kappa_2 = 0.03G$	Fig. 6(e)
(δ_1, δ_2)	$G_1 = G, G_2 = 5G$,	Fig. 6(b)
	$\kappa_1 = 0.3G, \kappa_2 = 1.5G$	Fig. 6(f)
(δ_1, G_2)	$G_1 = G, \delta_2 = 4G$,	Fig. 6(c)
	$\kappa_1 = 0.6G, \kappa_2 = 0.2G$	Fig. 6(g)
(δ_2, G_2)	$G_1 = G, \delta_1 = 10G$,	Fig. 6(d)
	$\kappa_1 = 0.7G, \kappa_2 = 0.01G$	Fig. 6(h)

FIG. 7. The instantaneous amplitudes of eigenstates and differential of the imaginary part of the effective Hamiltonian D_i during the loop evolution with two different independent variable sets. The evolution loop and other nonindependent parameters are the same as in Fig. 5(a). The blue solid (dashed) line describes the amplitude of the λ_+ (λ_-). The red dash-dotted line describes the differential of the imaginary part of λ_+ (λ_-). (a) The variable set is (δ_1, δ_2) and the other nonindependent parameters are the same as in Fig. 6(a). (b) The variable set is (G_1, G_2) and the other nonindependent parameters are the same as in Fig. 2(b).

branch cut of the topological structure of the Riemann sheet and the magnitude of D_i being 10^7. The amplitudes of $\lambda_{\pm}$ tend to approach each other when $\Gamma t/(\pi) \to 2$, corresponding to the magnitude of D_i, which is 10^6 and sufficiently large here. This phenomenon corresponds to the imaginary part of the dashed black line in Fig. 6(a), which is steepest in the last

four subgraphs in Fig. 6. When $\Gamma t/(\pi) \to 2$ in Fig. 7(b), it is clearly to find that the magnitude of D_i here is 10^3, which is sufficiently small for a state conversion to not occur. Based on comprehensive steepness and whether the large detuning conditions are easy to satisfy, variable sets (G_1, G_2) are chosen as the independent variables.

[1] B. Peng, Ş. K. Özdemir, F. Lei, F. Monifi, M. Gianfreda, G. L. Long, S. Fan, F. Nori, C. M. Bender, and L. Yang, Nat. Phys. **10**, 394 (2014).

[2] W. Chen, Ş. K. Özdemir, G. Zhao, J. Wiersig, and L. Yang, Nature (London) **548**, 192 (2017).

[3] W. D. Heiss, J. Phys. A: Math. Gen. **37**, 2455 (2004).

[4] J. Doppler, A. A. Mailybaev, J. Böhm, U. Kuhl, A. Girschik, F. Libisch, T. J. Milburn, P. Rabl, N. Moiseyev, and S. Rotter, Nature (London) **537**, 76 (2016).

[5] Y.-H. Lai, Y.-K. Lu, M.-G. Suh, Z. Yuan, and K. Vahala, Nature (London) **576**, 65 (2019).

[6] M. V. Berry and M. Wilkinson, Proc. R. Soc. London. A. Math. Phys. Sci. **392**, 15 (1984).

[7] J. Wiersig, Phys. Rev. Lett. **112**, 203901 (2014).

[8] H. Jing, Ş. K. Özdemir, X.-Y. Lü, J. Zhang, L. Yang, and F. Nori, Phys. Rev. Lett. **113**, 053604 (2014).

[9] J. Zhang, B. Peng, Ş. K. Özdemir, K. Pichler, D. O. Krimer, G. Zhao, F. Nori, Y.-x. Liu, S. Rotter, and L. Yang, Nat. Photon. **12**, 479 (2018).

[10] Y. Jiang, S. Maayani, T. Carmon, F. Nori, and H. Jing, Phys. Rev. Appl. **10**, 064037 (2018).

[11] G.-Q. Qin, M. Wang, J.-W. Wen, D. Ruan, and G.-L. Long, Photon. Res. **7**, 1440 (2019).

[12] J. Wiersig, Photon. Res. **8**, 1457 (2020).

[13] X. Mao, G.-Q. Qin, H. Yang, H. Zhang, M. Wang, and G.-L. Long, New J. Phys. **22**, 093009 (2020).

[14] G.-Q. Qin, R.-R. Xie, H. Zhang, Y.-Q. Hu, M. Wang, G.-Q. Li, H. Xu, F. Lei, D. Ruan, and G.-L. Long, Laser Photon. Rev. **15**, 2000569 (2021).

[15] H. Yang, X. Mao, G.-Q. Qin, M. Wang, H. Zhang, D. Ruan, and G.-L. Long, Opt. Lett. **46**, 4025 (2021).

[16] M.-A. Miri and A. Alù, Science **363**, eaar7709 (2019).

[17] J. W. Yoon, Y. Choi, C. Hahn, G. Kim, S. H. Song, K.-Y. Yang, J. Y. Lee, Y. Kim, C. S. Lee, J. K. Shin, H.-S. Lee, and P. Berini, Nature (London) **562**, 86 (2018).

[18] Q. Zhong, Ş. K. Özdemir, A. Eisfeld, A. Metelmann, and R. El-Ganainy, Phys. Rev. Appl. **13**, 014070 (2020).

[19] H. Xu, D. Mason, L. Jiang, and J. G. E. Harris, Nature (London) **537**, 80 (2016).

[20] D. Heiss, Nat. Phys. **12**, 823 (2016).

[21] A. U. Hassan, B. Zhen, M. Soljačić, M. Khajavikhan, and D. N. Christodoulides, Phys. Rev. Lett. **118**, 093002 (2017).

[22] X.-L. Zhang, T. Jiang, and C. T. Chan, Light Sci. Appl. **8**, 88 (2019).

[23] Q. Liu, S. Li, B. Wang, S. Ke, C. Qin, K. Wang, W. Liu, D. Gao, P. Berini, and P. Lu, Phys. Rev. Lett. **124**, 153903 (2020).

[24] S. Ke, B. Wang, C. Qin, H. Long, K. Wang, and P. Lu, J. Lightwave Technol. **34**, 5258 (2016).

[25] Q. Song, M. Odeh, J. Zúñiga-Pére, B. Kanté, and P. Genevet, Science **373**, 1133 (2021).

[26] K. J. Vahala, Nature (London) **424**, 839 (2003).

[27] S. R. K. C. Indukuri, J. Bar-David, N. Mazurski, and U. Levy, ACS Nano **13**, 11770 (2019).

[28] A. Li, J. Dong, J. Wang, Z. Cheng, J. S. Ho, D. Zhang, J. Wen, X.-L. Zhang, C. T. Chan, A. Alù, C.-W. Qiu, and L. Chen, Phys. Rev. Lett. **125**, 187403 (2020).

[29] W. D. Heiss and H. L. Harney, European Phys. J. D - Atom. Molec. Opt. Plasma Phys. **17**, 149 (2001).

[30] B. Peng, Ş. K. Özdemir, W. Chen, F. Nori, and L. Yang, Nat. Commun. **5**, 5082 (2014).

[31] J. Li, R. Yu, and Y. Wu, Phys. Rev. A **92**, 053837 (2015).

[32] M. Aspelmeyer, T. J. Kippenberg, and F. Marquardt, Rev. Mod. Phys. **86**, 1391 (2014).

[33] Y.-D. Wang and A. A. Clerk, Phys. Rev. Lett. **108**, 153603 (2012).

[34] L. Tian, Phys. Rev. Lett. **108**, 153604 (2012).

[35] Y.-C. Liu, Y.-F. Xiao, X. Luan, and C. W. Wong, Phys. Rev. Lett. **110**, 153606 (2013).

[36] J.-Q. Liao and F. Nori, Phys. Rev. A **88**, 023853 (2013).

[37] Z.-q. Yin, T. Li, X. Zhang, and L. M. Duan, Phys. Rev. A **88**, 033614 (2013).

[38] X.-Y. Lü, H. Jing, J.-Y. Ma, and Y. Wu, Phys. Rev. Lett. **114**, 253601 (2015).

[39] C. Cao, S.-C. Mi, Y.-P. Gao, L.-Y. He, D. Yang, T.-J. Wang, R. Zhang, and C. Wang, Sci. Rep. **6**, 22920 (2016).

[40] Z. Shen, Y.-L. Zhang, Y. Chen, F.-W. Sun, X.-B. Zou, G.-C. Guo, C.-L. Zou, and C.-H. Dong, Nat. Commun. **9**, 1797 (2018).

[41] X. Mao, G.-Q. Qin, H. Yang, Z. Wang, M. Wang, G.-Q. Li, P. Xue, and G.-L. Long, Phys. Rev. A **105**, 033526 (2022).

[42] K.-W. Xiao, A. Xiong, N. Zhao, and Z.-q. Yin, Quantum Eng. **3**, e62 (2021).

[43] C. Dong, V. Fiore, M. C. Kuzyk, and H. Wang, Science **338**, 1609 (2012).

[44] H.-K. Li, X.-X. Ren, Y.-C. Liu, and Y.-F. Xiao, Phys. Rev. A **88**, 053850 (2013).

[45] H. Zhang, X.-K. Song, Q. Ai, H. Wang, G.-J. Yang, and F.-G. Deng, Opt. Express **27**, 7384 (2019).

[46] T. J. Milburn, J. Doppler, C. A. Holmes, S. Portolan, S. Rotter, and P. Rabl, Phys. Rev. A **92**, 052124 (2015).

[47] P. Yin, X. Luo, L. Zhang, S. Lin, T. Tian, R. Li, Z. Wang, C. Duan, P. Huang, and J. Du, Chin. Phys. Lett. **37**, 100301 (2020).

[48] X.-L. Zhang, S. Wang, B. Hou, and C. T. Chan, Phys. Rev. X **8**, 021066 (2018).